

High temperature magnetism and microstructure of semiconducting ferromagnetic alloy $(\text{GaSb})_{1-x}(\text{MnSb})_x$

L.N. Oveshnikov^{1,2,*}, E.I. Nekhaeva^{1,2}, A.V. Kochura³, A.B. Davydov², M.A. Shakhov^{4,5}, S.F. Marenkin⁶, O.A. Novodvorskiy⁷, A.P. Kuzmenko³, A.L. Vasiliev¹, B.A. Aronzon^{1,2} and E. Lahderanta⁴

¹ *National Research Center "Kurchatov Institute", 123182 Moscow, Russian Federation*

² *P.N. Lebedev Physical Institute, Russian Academy of Sciences, 119991 Moscow, Russian Federation*

³ *South-West State University, 305040 Kursk, Russian Federation*

⁴ *Lappeenranta University of Technology, 53850 Lappeenranta, Finland*

⁵ *Ioffe Institute, 194021 St.Petersburg, Russian Federation*

⁶ *Kurnakov Institute of General and Inorganic Chemistry, Russian Academy of Sciences, 119991 Moscow, Russian Federation and*

⁷ *Institute on Laser and Information Technologies, Russian Academy of Sciences, 140700 Shatura, Moscow Region, Russian Federation*

We have studied the properties of relatively thick (about 120 nm) magnetic composite films grown by pulsed laser deposition method using $(\text{GaSb})_{0.59}(\text{MnSb})_{0.41}$ eutectic compound as a target for sputtering. For the studied films we have observed ferromagnetism and anomalous Hall effect above the room temperature, it manifests the presence of spin-polarized carriers. Electron microscopy, atomic and magnetic force microscopy results suggests that films under study have homogenous columnar structure in the bulk while MnSb inclusions accumulate near it's surface. This is in good agreement with high mobility values of charge carriers. Based on our data we conclude that room temperature magnetic and magnetotransport properties of the films are defined by MnSb inclusions.

I. INTRODUCTION

The diluted magnetic semiconductors (DMS) are very promising materials for spintronic devices, because DMS offer the combination of magnetic and semiconducting properties. Currently the most widely studied DMS systems are those based on III-V semiconductors doped by Mn¹⁻³. Among these systems the most known and better studied is $\text{Ga}_{1-x}\text{Mn}_x\text{As}$. Here Mn substitute Ga atoms and establish a ferromagnetic state realized via carrier-induced indirect exchange between Mn atoms by Zener - RKKY mechanism accompanied by the spin polarization of conducting holes^{1,3}. To reach high T_c values one needs material with high Mn concentration, which can be achieved by using non-equilibrium growth methods, such as low-temperature molecular-beam epitaxy. In particular, it increases the solubility limit of Mn in $\text{Ga}_{1-x}\text{Mn}_x\text{As}$ up to $x = 0.2$ without precipitate formation⁴. The highest Curie temperature T_c achieved in these materials was below 200 K, observed with x about 0.1^{5,6}. This is remarkably high for a DMS system while for practical applications is desired $T_c > 300$ K. At higher concentrations Mn atoms start to occupy interstitial sites and produce strong structure defects that increase scattering of charge carriers. Thus, hole mobilities in $\text{Ga}_{1-x}\text{Mn}_x\text{As}$ systems with high T_c ($x > 0.06$) usually do not exceed $10 \text{ cm}^2/(\text{V}\cdot\text{s})$.

Another way to realize high T_c in magnetic semiconductor material is to create a granular system with two phases, i.e. ferromagnetic nanoinclusions embedded into semiconductor matrix. Although, this type of systems are studied less often, in some of the related works observed T_c exceeded room temperature⁷⁻¹³. Additional advantage of granular systems is higher values of carrier mobility, about one order of magnitude higher than that

in traditional DMS such as $\text{Ga}_{1-x}\text{Mn}_x\text{As}$. That is due to the aggregation of the most part of magnetic impurity atoms within nanoinclusions, which results in higher crystalline quality of semiconductor matrix⁹ and lower density of scatterers. Thus, granular materials could be of interest, both as an object of fundamental studies of DMS systems and as a versatile material suitable for testing prototype spintronic devices.

Recent studies of MnAs inclusions embedded into GaAs matrix showed that inclusions can emerge with two types of crystal structure. Furthermore, the magnetic properties of MnAs inclusions with zinc blende type and hexagonal lattices are substantially different. That is why the actual application of GaAs:MnAs material is restricted by this obstacle.

Second recently studied nanocomposite system is GaSb matrix with incorporated MnSb nanograins^{8-10,14}. However, the best results were obtained not for a composite system but for the $(\text{GaSb})_{1-x}(\text{MnSb})_x$ alloys with $x = 0.41$. In particular, for annealed samples the mobility of holes was about $100 \text{ cm}^2/(\text{V}\cdot\text{s})$ and the T_c was above room temperature^{11,12}. Earlier it was suggested⁹ that the ferromagnetic ordering in this case is induced by interaction of MnSb magnetic clusters with carriers inside the matrix. It should induce carrier spin-polarization and lead to the formation of long range ferromagnetic percolation cluster which includes both MnSb magnetic clusters and spin-polarized carriers. However, to check this assumption and to reveal the origin of the high temperature ferromagnetism in GaSb-MnSb alloys, one needs a detailed knowledge of the sample structure.

Thus, in this paper we investigate magnetic and transport properties of the GaSb-MnSb alloy films with $x = 0.41$ and we elucidate the origin of the ferromagnetic state in this material. We use Atomic Force and Mag-

netic Force Microscopy (AFM and MFM) as well as scanning/transmission electron microscopy (S/TEM) to study the samples structure.

II. SAMPLES AND METHODS

GaSb-MnSb films with thickness (d) in the range between 120 nm and 135 nm and an area of $0.1 - 1 \text{ cm}^2$ were grown by the droplet-free pulsed laser deposition (PLD) method in a high vacuum of 10^{-6} Torr with deposition temperatures $T_{dep} = 100 - 300 \text{ }^\circ\text{C}$. We used GaSb-MnSb eutectic composition containing 41 mol.% MnSb and 59 mol.% GaSb as a target, that was sputtered by the second harmonic radiation of a Q-switched YAG:Nd laser ($\lambda = 532 \text{ nm}$). Al_2O_3 (0001) single crystals were used as substrates. More detailed description of the growth technology can be found in¹⁵.

Magnetization was measured at temperatures $T = 5 - 310 \text{ K}$ in magnetic fields up to $H = 50 \text{ kOe}$ using a superconducting quantum interference device (SQUID) magnetometer S600X (Cryogenic, UK). The electrical and magnetotransport properties were investigated at temperatures $T = 2 - 320 \text{ K}$ using standard six-probe geometry in pulsed magnetic fields up to $H = 300 \text{ kOe}$. Studied samples demonstrated linear current-voltage characteristics down to sub-helium temperatures while sustaining high values of conductivity.

The cross-section specimens for S/TEM studies was prepared by focus ion beam (FIB) milling procedure in a Helios (FEI, US) scanning electron microscope (SEM)/FIB dual beam system equipped with C and Pt contain gas injectors and a micromanipulator (Omniprobe, US). A $2 \text{ }\mu\text{m}$ Pt layer was deposited on the surface of the sample prior to the cross-sections preparation by FIB milling procedure. Sections of approximately $8 \times 5 \text{ }\mu\text{m}^2$ in size and $2 \text{ }\mu\text{m}$ thick were cut by 30 kV Ga⁺ ions, removed from the sample and then attached to the Omniprobe semiring (Omniprobe, US). Final thinning was performed with 5 kV Ga⁺ ions followed by cleaning by 2 keV Ga⁺ ions for the electron transparency. All specimens were studied in a scanning/transmission electron microscope (S/TEM) Titan 80-300 (FEI, US) equipped with a spherical aberration (Cs) corrector (electron probe corrector), a high-angle annular dark field (HAADF) detector, an atmospheric thin-window energy dispersive x-ray (EDX) spectrometer (Phoenix System, EDAX, US) and a post-column Gatan energy filter (GIF), (Gatan, US). The S/TEM was operated at 300 kV . Digital micrograph (Gatan, US) and TIA software (FEI, US) was used for image analysis. P.Stadelmann's JEMS software¹⁶ was used for diffraction patterns and image simulation.

Scanning atomic force microscopy (AFM) and magnetic force microscopy (MFM) images were obtained on an SmartSPM microscope (AIST-NT, US) at temperatures $T = 295 - 450 \text{ K}$.

TABLE I. Sample parameters: deposition temperature T_{dep} ; film thickness d ; carrier concentration p ; carrier mobility μ ; coercive force H_c ; remanent magnetization M_{rem} ; saturation magnetization M_{sat} (p , μ and M_{sat} were obtained at $T = 300 \text{ K}$, while H_c and M_{rem} values correspond to $T = 4.2 \text{ K}$).

Sample	T_{dep} , $^\circ\text{C}$	d , nm	p , 10^{19} cm^{-3}	μ , $\text{cm}^2/(\text{V} \cdot \text{s})$	H_c , [*] Oe	M_{rem} [*]	M_{sat} [*]
GM1	100	120	0.8	110	250	$1.4 \text{ }\mu_B$	$1.8 \text{ }\mu_B$
GM2	100	120	9.3	110	260	$2.1 \text{ }\mu_B$	$3.0 \text{ }\mu_B$
GM3	200	130	23	80	260	$1.7 \text{ }\mu_B$	$3.0 \text{ }\mu_B$
GM4	200	135	14	71	115	$2.1 \text{ }\mu_B$	$3.2 \text{ }\mu_B$
GM5	300	120	4.8	74	265	$0.6 \text{ }\mu_B$	$2.5 \text{ }\mu_B$

^{*}Magnetic parameters were obtained for magnetic field oriented parallel to the sample plain; magnetization were calculated per manganese atom.

III. RESULTS AND DISCUSSION

We have studied several $(\text{GaSb})_{1-x}(\text{MnSb})_x$ samples with $x = 0.41$, both annealed and not annealed. In this paper we discuss only samples annealed at $350 \text{ }^\circ\text{C}$ during 30 min with high holes concentration p ($> 10^{19} \text{ cm}^{-3}$) because they showed much better magnetic and semiconducting (electron transport) properties. Therefore, these samples are more suitable to reveal the nature of magnetic properties and hole spin-polarization in this material which is the aim of this paper. Main parameters of the studied samples are presented in the Table 1.

Fig. 1a shows typical curves of magnetization versus magnetic field for the sample GM3 (see Table 1) for magnetic field orientations in the sample plane and perpendicularly to it. The presence of well-pronounced hysteresis suggests that ferromagnetic ordering in these materials appears at $T > 300 \text{ K}$. This is more evident from the temperature dependence of the remanent magnetization M_{rem} presented in Fig. 1b. At the same figure we also provide the MFM data and temperature dependence of the remanent magnetization for InSb-MnSb eutectics. Nonzero M_{rem} persists up to 400 K and its temperature dependence is close to that for InSb-MnSb eutectic composition which corresponds to the MnSb $T_c \approx 600 \text{ K}$ ¹⁷. Thus, presented data clearly proves the presence of high temperature ferromagnetism in the samples under study.

As said earlier, studied systems differs from traditional DMS materials by substantially higher carrier mobilities and T_c values, while the nature of high temperature ferromagnetism is not completely clear. Previous studies⁹ suggested that ferromagnetism in $(\text{GaSb})_{1-x}(\text{MnSb})_x$ is related to the interaction of charge carriers with MnSb nanoinclusions with $T_c = 600 \text{ K}$ ^{17,18}. This interaction is affected by the appearance of Shottky barriers at the MnSb/GaSb boundaries. Basically, these type of barriers appear on the semiconductor/metal interfaces providing a tunneling charge transfer across the boundary, if the

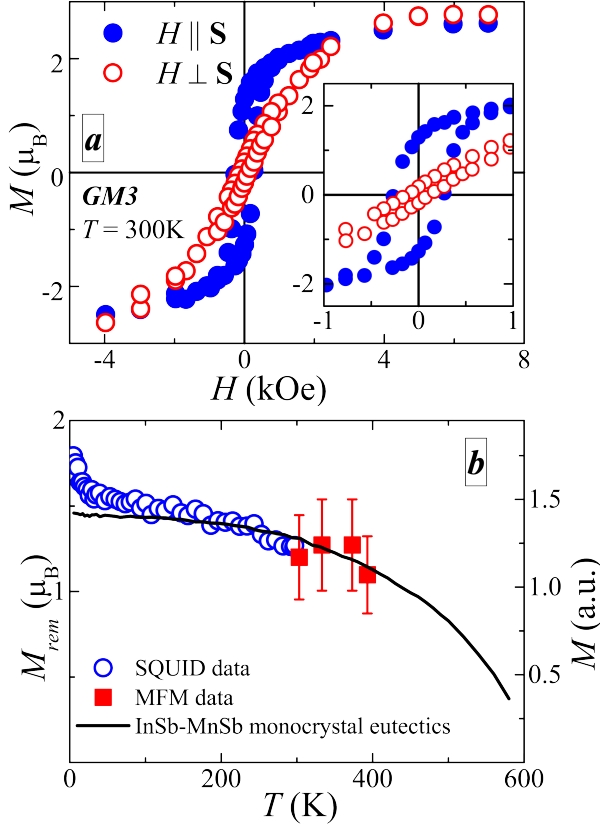


FIG. 1. (colour online) (a) Magnetization vs. magnetic field for sample GM3 at $T = 300$ K. Measurements were performed with magnetic field oriented in the sample plane (solid symbols) and perpendicular to it (open symbols). Inset demonstrate hysteresis loop at low fields. (b) Temperature dependence of the remanent magnetization. Open circles are SQUID data for sample GM3, red squares are MFM data for the same sample and black curve is temperature dependence of the saturation magnetization of InSb-MnSb eutectics¹⁷.

barrier is high enough. In the present case Shottky barriers may appear only if inclusions are sufficiently large to establish second electronic phase (metal-type) despite the impact of surrounding GaSb matrix. Parameters of these barriers (e.g. the width) substantially depend on charge distribution, i.e. they depend on carrier concentration.

It is worth mentioning that in real samples not all Mn atoms are strictly positioned in MnSb inclusions, some part of Mn atoms can be distributed within semiconductor matrix. It results in two-phase magnetic subsystem for which lower T_c corresponds to isolated Mn atoms within matrix¹⁹. Also, as it is shown in Table 1, the M_{sat} values reach $3.2 \mu_B$ per Mn atom which is close to $3.6 \mu_B$ value obtained from the experimental data for MnSb samples analyzed earlier^{18,21}, but is lower than expected for Mn^{2+} . This difference can be related to the presence of Mn^{3+} ions and antiferromagnetic character of interaction between carriers and Mn atoms.

One major parameter of holes interaction with MnSb

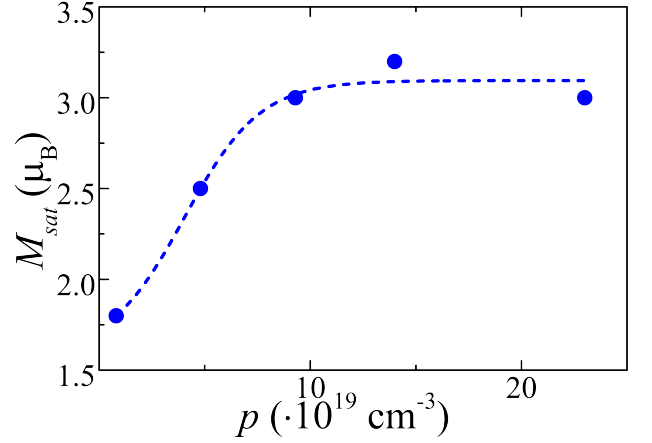


FIG. 2. (colour online) Room temperature saturation magnetization (M_{sat}) versus carrier concentration (p) dependence (dash line is a guide to the eye).

inclusions is the width of Shottky barriers $d_{barrier}$ which decreases with the growth of carrier concentration⁹. This picture correlates with concentration dependence of saturation magnetization M_{sat} presented in Fig. 2. This also agrees well with the data obtained for previously studied $(GaSb)_{1-x}(MnSb)_x$ films (see Fig. 5 in¹²). As it can be seen from these figures, M_{sat} increases with carrier concentration and saturates above $p \approx 10^{20} \text{ cm}^{-3}$ at which $d_{barrier}$ becomes comparable with the effective penetration depth of carrier (hole) wave function under triangular barrier l_p . Taking into account that energy gap in GaSb is $E_g = 0.7 \text{ eV}$ and the Schottky barrier height is about $1/3 E_g$ ²⁰, the $d_{barrier}$ can be estimated as 2 nm at $p = 10^{20} \text{ cm}^{-3}$ while l_p is of the same value⁹. As shown in Fig. 2, p values for studied samples are sufficiently high to provide effective holes interaction with MnSb inclusions and cause the saturation of magnetization. This, along with high T_c values, suggests that this interaction could be the main source of high temperature ferromagnetism in studied systems. However, to justify the applicability of carrier-to-inclusions interaction model one need to verify specific properties of spin-polarized system, e.g. displayed in transport measurements.

It should be noted, that mobility values have no pronounced dependence on carrier concentration (see Table 1), i.e. the conductivity of studied films is affected by various factors. Thus, magnetotransport phenomena can yield additional information on system properties. The results of Hall resistivity measurements for the GM3 sample are shown in Fig. 3a and 3b. The Hall resistivity in magnetic systems can be divided into two parts:

$$R_{xy} \cdot d = R_H \mathbf{H} + R_s \mathbf{M}, \quad (1)$$

where R_H is Hall constant, used for p and μ determination (see Table 1), and R_s is anomalous Hall constant, which is defined by several parameters of the system and corresponding mechanism²². Thus, the $R_{xy}(H)$ should reproduce field dependence of magnetization. As

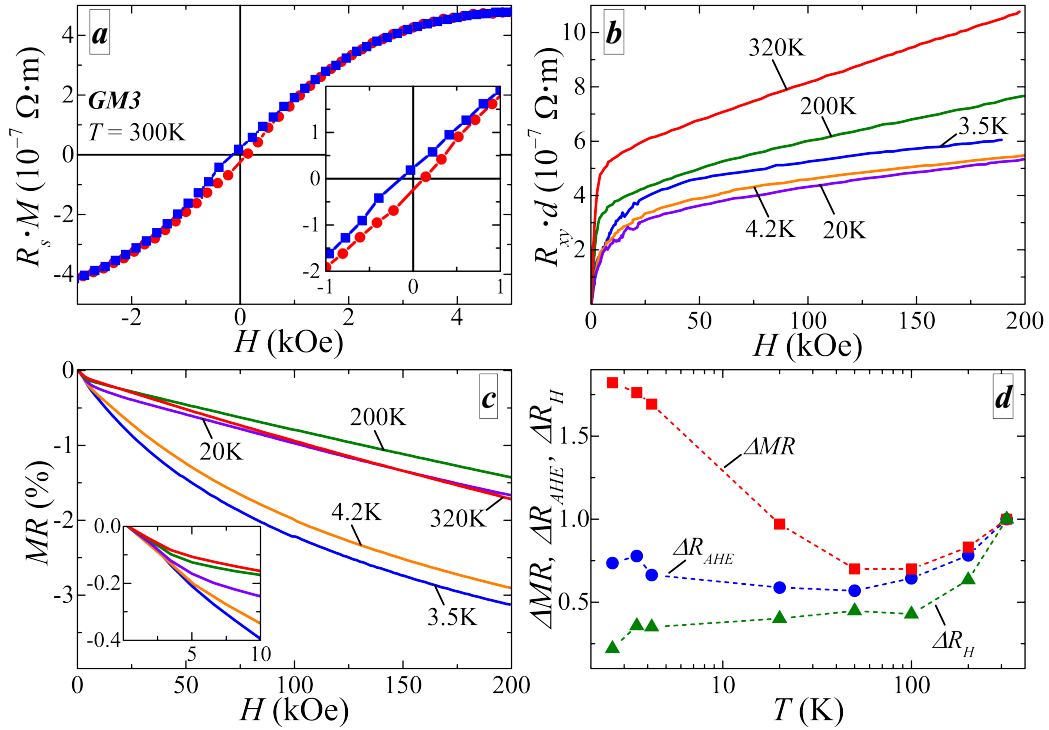


FIG. 3. (colour online) Magnetotransport properties of sample GM3: (a) Field dependence of anomalous Hall component at 300 K (here we have subtracted linear background). Slope of the curve correlates with the sign of charge carriers (holes), i.e. observed AHE is positive. Inset demonstrate hysteresis behaviour at low fields. (b) Field dependence of Hall resistance up to $H = 200$ kOe at various temperatures. (c) Magnetoresistance at various temperatures. Inset shows low field part of presented curves. (d) Temperature dependence of high field magnetoresistance ΔMR (at $H = 200$ kOe), saturated AHE amplitude ΔR_{AHE} and Hall slope ΔR_H normalized by corresponding values at $T = 320$ K.

it shown in Fig. 3a $R_s \cdot M(H)$ (Hall resistivity after subtraction of linear contribution) demonstrates hysteresis behavior (see inset) with $H_c \approx 140$ Oe and saturation field $H_{sat} \approx 3.8$ kOe. This is in a good agreement with values $H_c \approx 130$ Oe and $H_{sat} \approx 4$ kOe obtained from SQUID data for H perpendicular to the sample plain. Note, that H_c and H_{sat} values in Table 1 were obtained for H oriented parallel to the sample plain, thus, the difference between them and parameters obtained from $R_{xy}(H)$ curves is related to substantial magnetic anisotropy of samples under study (see Fig. 1). The observation of anomalous Hall effect (AHE) clearly suggests that delocalized holes interact with magnetic subsystem, i.e. there are spin-polarized carriers even at room temperature. Thus, the exchange interaction within studied system can be mediated by these spin-polarized holes as it was suggested earlier.

The incorporation of experimentally observed high-temperature ferromagnetism and spin polarization of conducting carriers already makes studied films very perspective for various applications. But to get a deeper insight into properties of these films we have made additional magnetotransport measurements in high magnetic fields. Hall resistivity dependencies in magnetic fields up to $H = 200$ kOe at various temperatures are presented in Fig. 3b. It is clearly seen that at room temperature

the anomalous Hall effect contribution saturates below $H = 10$ kOe and $R_{xy}(H)$ become linear. The linear slope and the saturation field are different for different temperatures. To visualise the temperature evolution of presented curves we used simple linear fit of high field region. In this case fitting function have two variables, slope (R_H) and an offset, which corresponds to saturated AHE amplitude R_{AHE} . Second common sign of interaction between magnetic and conducting subsystems is the appearance of negative magnetoresistance (nMR), which is usually ascribed to spin-dependent scattering. As it is shown in Fig. 3c studied samples demonstrate nMR which does not saturate up to 200 kOe in studied temperature interval. It should be noted, that at low field nMR have similar form at all temperatures (see inset in Fig. 3c), while at higher fields shape of MR curves changes. In particular, above 20 K nMR is linear above 20 kOe, while below 4.2 K the shape of nMR is close to sublinear or logarithmic, which is more common for spin-dependent scattering contribution^{23–25}.

Based on the assumption of two-phase magnetic subsystem (MnSb inclusions and isolated Mn atoms) we can qualitatively describe temperature evolution of magnetotransport parameters presented in Fig. 3d. The character of ΔR_{AHE} and ΔMR dependencies is rather similar, thus, they should have the same nature. At 50 K we ob-

serve local minimum in both curves. The increase above 50 K can be related to the presence of Shottky barriers, because, if both AHE and nMR corresponds to the interaction with MnSb inclusions, then their amplitudes are defined by tunneling intensity which increases with temperature. But below 50 K another contribution becomes significant, the interaction with isolated Mn moments. From our data we cannot define corresponding T_c accurately because this interaction can be significant even above the ordering temperature^{24,25}, while the total magnetic moment of isolated Mn atoms can be substantially smaller than that of MnSb inclusions. Temperature dependence of ΔR_H is more complicated. But in the present case of large AHE contribution, MR and AHE itself can strongly affect R_H through the relations of conductivity and resistivity tensors²⁶. It should be noted that nMR at high temperatures can be also due to tensor relations, although mentioned difference of nMR functional form at various temperatures suggests that, at least at low temperatures, nMR should be related to the spin-dependent scattering. Also there are several other phenomena that can be relevant. Thus, to elucidate their contributions a more thoughtful study with quantitative simulations is needed, but it is out of scope of present paper.

To establish high temperature ferromagnetism of MnSb inclusions via spin-polarized carriers their interaction have to be sufficiently strong. It implies that there have to be a large amount of such inclusions with distances between them less than carrier spin relaxation length. However, the comparatively high carrier mobilities in studied samples still leave some doubt on the mentioned idea, because big amount of MnSb inclusions (as well as high concentration of isolated Mn atoms) should induce intense scattering of carriers, i.e. low mobilities. The latter, according to estimates, should not exceed $10 \text{ cm}^2/(\text{V}\cdot\text{s})$, as it is in GaMnAs²⁷ and previously studied GaMnSb with highest T_c ⁹. This contradicts the suggestion that MnSb nanoinclusions are distributed over the whole volume of the film. Thus, a detailed knowledge of samples structure is required to resolve this problem properly. To get this information we performed additional measurements using S/TEM, AFM and MFM methods.

In the present TEM/EDX microanalysis study of the GaSb-MnSb/ $\alpha\text{-Al}_2\text{O}_3$ system the actual investigation was performed on the cross-sectional piece of sample GM3 with lateral sizes of about $1 \mu\text{m}$. Results are presented in Fig. 4a and 4b. The film thickness is about 150 nm and the surface roughness does not exceed 6 nm. This is in a good agreement with the data presented in Table 1, which were estimated from the duration of deposition process. The image analysis confirms homogeneous composition throughout the film thickness without any substantial contrast variations. Contrast changes in the lateral direction are due to diffraction contrast arising from the columnar film microstructure which was distinctly observed on bright-field TEM (Fig. 4a) and high-

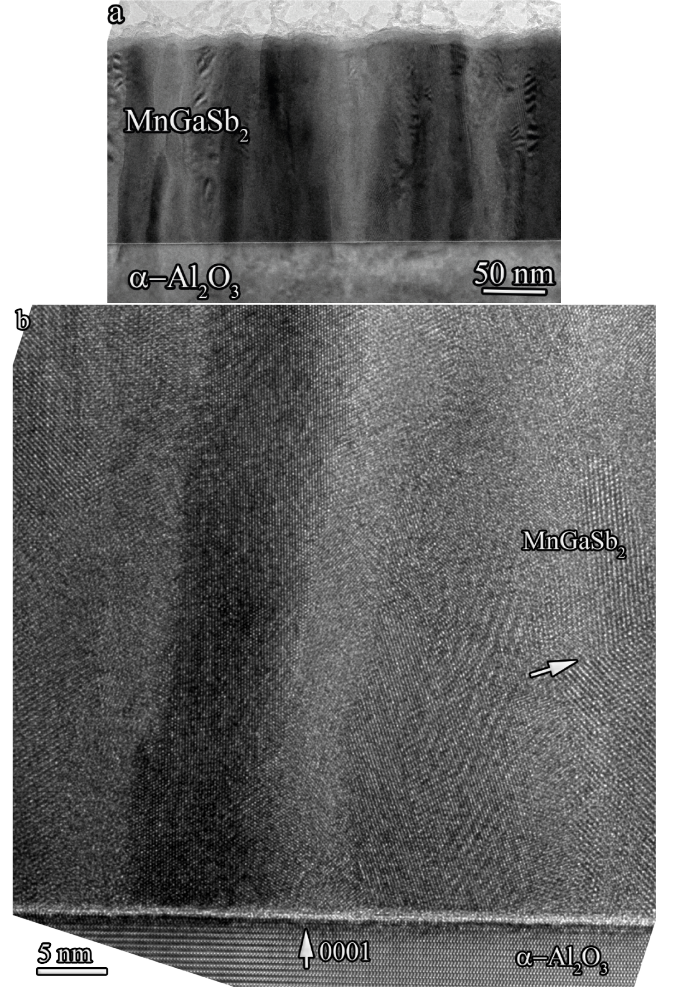


FIG. 4. TEM images of the film cross-section after annealing (sample GM3): (a) Bright field image. (b) HRTEM image.

resolution bright-field TEM (HRTEM) images (Fig. 4b), and even effect the HAADF TEM image (not presented here).

Energy-dispersive X-ray microanalysis (EDX) study of the film composition near the interface edge and at a distance from it yielded the ratio Mn:Ga:Sb=30:30:40 with 2% accuracy. HRTEM image of studied film is presented in Fig.4b. Fast Fourier Transform (FFT) analysis of high-resolution image areas in two directions (Fig. 5b and 5e) and direct analysis of crystal cell image (Fig. 5c and 5f) were used to analyze the crystalline structure of the sample. As an example, the results for two of ten studied image areas are presented in Fig. 5.

The analysis of all studied areas unambiguously indicate that the structure of the film is cubic and corresponds to the structural type of the GaSb crystal lattice (*space group* $F\bar{4}3m$). Moreover, the images clearly show twins and stacking faults, which are typical for the cubic GaSb crystals. At the same time, the electron diffraction data obtained for pristine films correspond to diffraction patterns for the hexagonal compound with the *space*

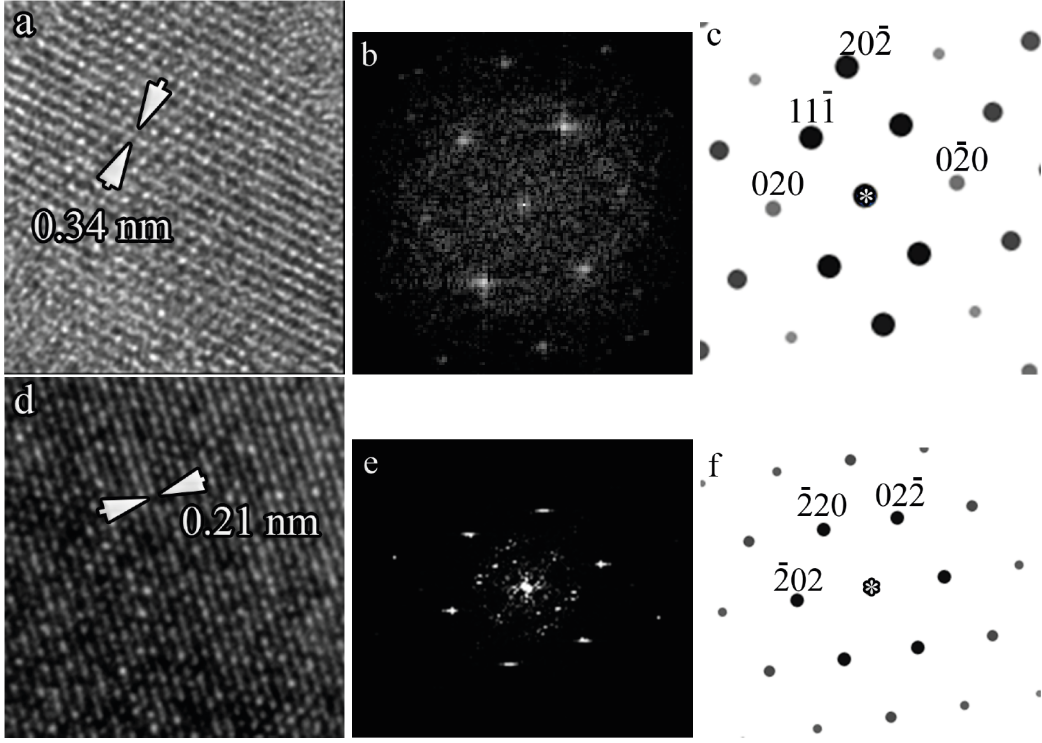


FIG. 5. (a,d) HRTEM images of sample areas. (b,e) Corresponding two-dimensional Fourier spectra. (c,f) Calculated electronograms of cubic MnGaSb_2 compound in $[101]$ (c) and $[111]$ (f) projections.

group $P6^3/mmc$. Also, the image analysis showed that the morphology of the film and the lateral dimensions of the film columns remained the same after annealing. It should be noted, that energy-dispersive X-ray microanalysis showed a slight (2-3%) decrease of Mn content in the film volume after annealing. This can be related to the details of sample preparation (e.g. the presence of a thicker damaged layer on the surface) or to the diffusion of Mn atoms. Thus, we can conclude that film annealing causes a phase transition of the hexagonal GaSb matrix to cubic one. As a result, the electron microscopy data unambiguously shows that the columnar microstructure of the film persists up to almost surface layers. It should be noted, that no signs of second phase precipitates in the film volume was observed. In particular, using a GaSb-MnSb eutectic composition as a target for sputtering allowed us to avoid MnGa inclusion formation, which were observed earlier in samples obtained by laser deposition from Mn and GaSb targets, without taking the stoichiometry into account²⁸.

However, due to unevenness of the film and oxidation, the top layer of the film could not be studied carefully and we cannot determine the exact morphology and composition of the surface. So the AFM and MFM measurements were performed.

AFM and MFM images of one sample obtained at 303 and 413 K are presented in Fig. 6. The MFM images clearly show that magnetic properties of the system remain stable at these temperatures, i.e. the sample ex-

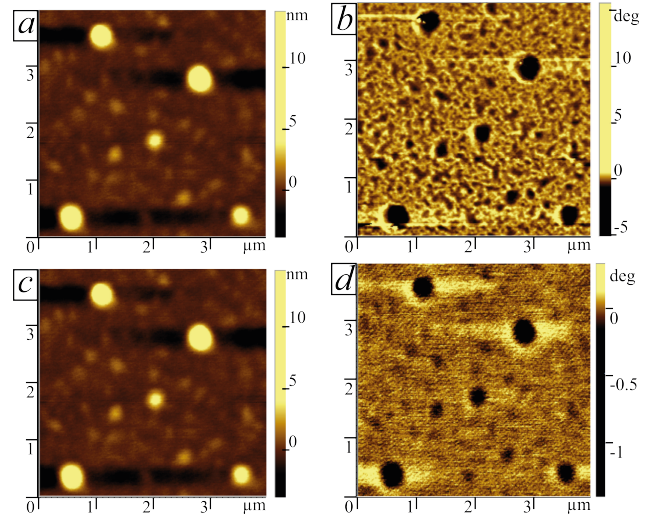


FIG. 6. (colour online) AFM (a,c) and MFM (b,d) images of the same surface at 303 K (a,b) and 413 K (c,d).

hibits ferromagnetism with T_c much higher than room temperature. A comparison of the AFM and MFM data shows that magnetic moments are distributed mostly within areas of larger height (MnSb inclusions) detected by AFM. Combining these results with SEM and TEM data suggests that MnSb inclusions are ferromagnetic and located mostly close to the film surface, rather than

evenly distributed within its volume. This assumption also provides a good explanation of high mobility values of conducting holes, since magnetic inclusions localized on the surface have a substantially weaker effect on scattering in studied films.

IV. CONCLUSIONS

We have studied structural, magnetic and magnetotransport properties of annealed $(\text{GaSb})_{1-x}(\text{MnSb})_x$ films with $x = 0.41$ and thickness $d = 120\text{--}135$ nm. Electron microscopy data suggests that studied films have single-phase columnar structure in its volume. Moreover, it was found that annealing process induce phase transition of hexagonal GaSb matrix into cubic one. On the other hand, AFM and MFM studies revealed the presence of ferromagnetic MnSb inclusions near surface of the films. This perfectly explains high mobility values of charge carriers in these systems. Experimental obser-

vation of these inclusions is crucial for the explanation of high temperature ferromagnetism, since magnetization hysteresis at room temperature perfectly fits the idea of dominant contribution of MnSb inclusions with $T_c > 400$ K interacting via holes. It is confirmed by the appearance of substantial anomalous Hall effect even at room temperature. The interaction of charge carriers with inclusions is greatly affected by the Shottky barriers on GaSb/MnSb boundaries. Due to high carrier concentrations in studied films, the transparency of these barriers is rather high which explains the saturation of magnetization at $p = 10^{20} \text{ cm}^{-3}$.

V. ACKNOWLEDGEMENTS

This work was partially supported by Russian Foundation for Basic Research (grants #17-02-00262 and #16-03-00150) and by Ministry of Education and Science of Russian Federation (grant #16.2814.2017/PCh).

-
- ¹ Jungwirth T, Sinova J, Masek J, Kucera J, MacDonald A H 2006 *Rev. Mod. Phys.* **78** 809-864
 - ² Dietl T 2007 *Lecture Notes on Semiconductor Spintronics* vol. 712 (Berlin: Springer) pp 1-46
 - ³ Dietl T, Ohno H 2014 *Rev. Mod. Phys.* **86** 187-251
 - ⁴ Chen L, Yan S, Xu P F, Lu J, Wang W Z, Deng J J, Qian X, Ji Y, Zhao J H 2009 *Appl. Phys. Lett.* **95**(18) 182505
 - ⁵ Wang M, Marshall R A, Edmonds K W, Rushforth A W, Campion R P, Gallagher B L 2014 *Appl. Phys. Lett.* **104** 132406
 - ⁶ Chen L, Yang X, Yang F, Zhao J, Misuraca J, Xiong P, von Molnar S 2011 *Nano Lett.* **11**(7) 2584-2589
 - ⁷ Lawniczak-Jablonska K, Libera J, Wolska A, Klepka M T, Dłuzewski P, Sadowski J, Wasik D, Twardowski A, Kwiatkowski A, Sato K 2011 *Phys. Status Solidi RRL* **5** 62-64
 - ⁸ Lawniczak-Jablonska K, Wolska A, Klepka M T, Kret S, Gosk J, Twardowski A, Wasik D, Kwiatkowski A, Kurowska B, Kowalski B J, Sadowski J 2011 *J. Appl. Phys.* **109** 074308
 - ⁹ Rylkov V V, Aronzon B A, Danilov Yu A, Drozdov Yu N, Lesnikov V P, Maslakov K I, Podol'skii V V 2005 *J. Exp. Theor. Phys.* **100**(4) 742
 - ¹⁰ Braun W, Trampert A, Kaganer V M, Jenichen B, Satapathy D K, Ploog K H 2007 *J. of Cryst. Growth* **301** 50-53
 - ¹¹ Marenkin S F, Novodvorsky O A, Shorokhova A V, Davydov A B, Aronzon B A, Kochura A V, Fedorchenko I V, Khramova O D, Timofeev A V 2014 *Inorg. Mater.* **50**(9) 897
 - ¹² Koplak O V, Polyakov A A, Davydov A B, Morgunov R B, Talantsev A D, Kochura A V, Fedorchenko I V, Novodvorsky O A, Shorokhova A V, Aronzon B A 2015 *J. Exp. Theor. Phys.* **120**(6) 1012-1018
 - ¹³ Talantsev A, Koplak O, Morgunov R 2016 *Superlattices and Microstructures* **95** 14-23
 - ¹⁴ Matsukura F, Abe E, Ohno H 2000 *J. Appl. Phys.* **87**(9) 6442-6444
 - ¹⁵ Lotin A A, Novodvorsky O A, Khaydukov E V, Rocheva V V, Khramova O D, Panchenko V Ya, Wenzel C, Trumpaicka N, Shcherbachev K D 2010 *Semiconductors* **44** 246
 - ¹⁶ Stadelmann P A 1987 *Ultramicroscopy* **21** 131
 - ¹⁷ Novotortsev V M, Kochura A V, Marenkin S F, Fedorchenko I V, Drogunov S V, Lashkul A, Lahderanta E 2011 *Russian Journal of Inorganic Chemistry* **56**(12) 1951-1956
 - ¹⁸ Teramoto I, Van Run A M J G 1968 *J. Phys. Chem. Solids.* **29** 347-352
 - ¹⁹ Yakovleva E I, Oveshnikov L N, Kochura A V, Lisunov K G, Lahderanta E, Aronzon B A 2016 *J. Exp. Theor. Phys. Lett.* **101**(2) 130-135
 - ²⁰ Sze S 1981 *Physics of Semiconductor Devices* 2nd ed. (New York: Wiley) p 880
 - ²¹ Coehoorn R, Haas C, Groot R A 1985 *Phys. Rev. B* **31** 1980
 - ²² Nagaosa N, Sinova J, Onoda S, MacDonald A H, Ong N P 2010 *Rev. Mod. Phys.* **82** 1539
 - ²³ Xiao J Q, Jiang J S, Chien C L 1992 *Phys. Rev. Lett.* **68**(25) 3749-3752
 - ²⁴ Oveshnikov L N, Kulbachinskii V A, Davydov A B, Aronzon B A, Rozhansky I V, Averkiev N S, Kugel K I, Tripathi V 2015 *Scientific Reports* **5** 17158.
 - ²⁵ Oveshnikov L N, Nekhaeva E I 2017 *Semiconductors* **51**(10) 1313-1320
 - ²⁶ Shen S, Liu X, Ge Z, Furdyna J K, Dobrowolska M, Jaroszynski J 2008 *J. Appl. Phys.* **103**(7) 07D134
 - ²⁷ Hayashi T, Tanaka M, Nishinaga T, Shimada H 1997 *J. Appl. Phys.* **81**(8) 4865-4867
 - ²⁸ Bobrov A I, Pavlova E D, Kudrin A V, Malekhonova N V 2013 *Semiconductors* **47**(12) 1587-1590